ChemCatChem
Full Papers
doi.org/10.1002/cctc.202100292
Chemistry Europe
European Chemical Societies Publishing

Rhodium Single-Atom Catalysts on Titania for Reverse Water Gas Shift Reaction Explored by First Principles Mechanistic Analysis and Compared to Nanoclusters

Francis Doherty[a, b] and Bryan R. Goldsmith*[a, b]

The thermocatalytic reduction of CO_2 by H_2 often proceeds via two competing reaction mechanisms – the reverse water gas shift reaction (rWGSR, $CO_2+H_2 \rightleftharpoons CO+H_2O$) and methanation ($CO_2+4H_2 \rightleftharpoons CH_4+2H_2O$). Atomically dispersed Rh_1 catalysts on TiO_2 show high selectivity toward the rWGSR compared with larger Rh nanoclusters, but the origin of this size-dependent selectivity has not been fully explained. Here we report density functional theory (DFT) calculations and microkinetic simulations that clarify the Rh_1 active sites and rWGSR pathway on anatase $TiO_2(101)$, as well as the high rWGSR selectivity of Rh_1 compared with supported Rh_x ($x=2$–8 atoms) nanoclusters. DFT-computed formation energies, vibrational frequency analysis, and microkinetic modeling suggest three plausible active sites: Rh_1 on titania ($Rh_1/TiO_2(101)$), Rh_1 with a nearby hydroxyl group ($Rh_1OH/TiO_2(101)$), and Rh_1 near an oxygen vacancy at a three-fold coordinated site (Rh_1 near O_{3c}vac). Predicted turnover frequencies and apparent activation barriers for Rh_1 indicate a faster reaction involving CO_2 dissociation assisted by a support oxygen vacancy via Rh_1 near O_{3c}vac, as well as slower reactions involving $Rh_1OH/TiO_2(101)$ or $Rh_1/TiO_2(101)$ through a COOH intermediate. These Rh_1 sites are selective toward CO rather than CH_4 because of the weak adsorption of CO, large barrier for C–O bond dissociation, and the lack of nearby metal sites for H_2 dissociation, in contrast to Rh_x nanoclusters, including Rh_2 dimers.

Introduction

The size of supported nanoparticles affects catalytic performance for many reactions, such as CO oxidation,[1] methane activation,[2] and CO_2 reduction.[3,4] Taking this size-dependent catalytic phenomenon to the limit, researchers have been developing atomically dispersed (i.e., single atom) catalysts, which frequently show modified activity and selectivity relative to their larger nanocluster (<2 nm) or nanoparticle counterparts.[5–8] Importantly, atomically dispersed catalysts can also achieve the maximum possible dispersion of metal on a support, making optimal use of rare and expensive metals.

In some cases, atomically dispersed catalysts are more active or selective than nanoclusters. For example, the direct conversion of methane to methanol was achieved with high selectivity by using atomically dispersed rhodium supported on titanium dioxide (Rh_1/TiO_2).[9] In other cases, nanoclusters display higher activity than atomically dispersed catalysts (e.g., Pt/CeO_2 for low-temperature CO oxidation).[10] Nevertheless, the activity and selectivity differences between nanoclusters and their atomically dispersed counterparts are not well-understood for many reactions.[11]

One reaction where atomically dispersed catalysts and their corresponding nanoclusters have shown different activity and selectivity is the thermocatalytic reduction of CO_2 by H_2, which has become an intensively studied area of research because of environmental concerns.[12,13] Thermocatalytic CO_2 reduction can occur via the reverse water gas shift reaction (rWGSR, $CO_2+H_2 \rightleftharpoons CO+H_2O$) or catalytic methanation ($CO_2+4H_2 \rightleftharpoons CH_4+2H_2O$) depending on the reaction conditions and catalyst. Methanol synthesis from the hydrogenation of CO_2 is also an important reaction for improving the chemical industry's environmental impact,[11] but is hindered by the competing rWGSR.

Notably, the activity and selectivity of CO_2 reduction to products such as methane and CO depends strongly on the metal catalyst size.[4,14,15] In particular, CO_2 reduction by Rh/TiO_2 displays a strong selectivity dependence between CO vs. CH_4 on the fraction of atomically dispersed Rh_1 relative to Rh nanoclusters. Correlations were observed between catalytic methanation turnover frequency (TOF) and the fraction of Rh nanoclusters, and between the TOF of the rWGSR and the fraction of Rh_1 species.[3] These Rh_1 species can be synthesized via techniques such as strong electrostatic adsorption[16–18] and atomic layer deposition,[19,20] or can spontaneously form via Rh nanocluster disintegration under reaction conditions.[21–27] The Rh_1 species are typically detected as gem-dicarbonyl $Rh_1(CO)_2$ complexes via diffuse reflectance Fourier transform infrared

---

[a] *F. Doherty, Prof. B. R. Goldsmith*
Department of Chemical Engineering
University of Michigan
2300 Hayward St.
Ann Arbor, MI 48109-2136 (USA)
E-mail: bgoldsm@umich.edu
[b] *F. Doherty, Prof. B. R. Goldsmith*
Catalysis Science and Technology Institute
University of Michigan
2300 Hayward St.
Ann Arbor, MI 48109-2136 (USA)

Supporting information for this article is available on the WWW under https://doi.org/10.1002/cctc.202100292

This publication is part of a Special Collection on "Computational Catalysis". Please check the ChemCatChem homepage for more articles in the collection.

spectroscopy (DRIFTS)[3,28] and may anchor on the surface oxygen or in oxygen vacancies on metal oxide supports.[29–32] Stable Rh_1 species coexist with Rh particles on TiO_2 with ratios that depend on the loading percent of Rh, temperature, and gas composition.

The large difference in selectivity between Rh_1 species and Rh nanoclusters toward the rWGSR is not well-understood at the atomic level, in part due to a lack of knowledge of the precise active sites and elementary reaction steps. Several rWGSR mechanisms for Rh_1 on vacancy-free anatase $TiO_2(101)$ were explored based on electronic energies predicted using density functional theory (DFT) modeling.[33] The high selectivity of Rh_1 toward CO was proposed to arise from a lack of orbital overlap between the highest occupied molecular orbital of Rh_1 and the lowest unoccupied molecular orbital of H_2, which prevents H_2 adsorption on Rh_1 while CO is bound and halts the reaction before hydrogenation to CH_4.[33] However, the predicted rWGSR mechanism includes a large activation barrier of 1.9 eV for the second elementary hydrogenation step to form the CO and H_2O from the commonly proposed carboxyl (*COOH) intermediate.[34,35] Ir_1/FeO_x, Ru_1/Al_2O_3, and Pt_1/FeO_x have similar TOFs as Rh_1/TiO_2 for CO_2 reduction (i.e., TOF of 0.005–0.03 s^{-1} at 473 K),[3] with measured apparent activation energies around 0.52–0.82 eV between 270–350 K,[36,37] suggesting alternative reaction pathways or different Rh_1 catalytic sites may be responsible for the observed activity and selectivity differences compared with Rh nanoclusters. Further atomistic modeling of the rWGSR on Rh_1/TiO_2 and Rh nanoclusters would clarify the origin for the rWGSR activity and selectivity differences with particle size.

Here we report first-principles modeling studies of Rh_1 sites and small Rh_x nanoclusters ($x=2$–8) on anatase TiO_2 to understand the activity of Rh_1 sites toward rWGSR and to explain the high selectivity of Rh_1 toward rWGSR compared to nanoclusters. Plausible Rh_1 active sites on anatase TiO_2 for rWGSR are identified based on DFT-predicted formation energies, gem-dicarbonyl vibrational frequency analysis, and microkinetic modeling. Rh_1 near an oxygen vacancy at a three-fold coordinated site (Rh_1 near O_{3c}vac) is predicted to be the most active Rh_1 site because the nearby oxygen vacancy helps activate CO_2, yielding faster kinetics than proceeding through a *COOH intermediate. Rh_1 species on TiO_2 are found to be more selective toward rWGSR than Rh_x/TiO_2 nanoclusters because (i) CO adsorbs weaker to Rh and has a stronger C–O bond strength on all Rh_1 sites compared with nanoclusters, and (ii) Rh_1 active sites have a higher barrier for H_2 dissociation and adsorb hydrogen weaker than nanoclusters. The Rh_1 sites are predicted to be unique in their ability to have high selectivity toward CO even compared to Rh_2 dimers.

Computational Methods

DFT calculations. All DFT calculations were conducted using the Vienna Ab initio Simulation Package.[38–40] Electron-ion interactions were treated with the projector augmented-wave method.[41] Anatase $TiO_2(101)$ was studied because the anatase phase is more stable than rutile for high-surface area particles smaller than ~14 nm.[42,43] The (101) surface was selected because it is the most abundant facet of the anatase surface.[44] A five-layer thick anatase $TiO_2(101)$ slab (1×3 surface, 174 atoms total) with a 20 Å vacuum layer was built in the Atomic Simulation Environment (ASE).[45] Bulk experimental lattice constants of 3.78 Å (*a*, *b*) and 9.51 Å (*c*) were specified for the $TiO_2(101)$ model.[46] The bottom two layers of the $TiO_2(101)$ slab were fixed in the position of the bulk lattice, whereas the top three layers could relax during geometry optimization. The (134) surface, which exhibits (100)-like facets between steps, was chosen as a step-edge model. The (134) model was constructed as a 1×3 periodic surface slab that was three layers thick (192 atoms total). The top two layers of the (134) slab could relax during geometry optimization. Dipole corrections were included in the *z* direction for each model surface. A plane wave basis set with a cutoff energy of 340 eV was selected after benchmarking. The *k*-space was sampled using a 4×4×1 Monkhorst-Pack grid. Transition states were found using the Climbing Image Nudged Elastic Band method.[47]

The PBE+U functional with the D3 dispersion[48] correction was used for all calculations.[49,50] DFT using only PBE fails to describe the strong on-site Coulomb interaction of localized *d*-electrons in TiO_2, so a U value of 2.5 eV was chosen to reproduce the reaction energy of O vacancy formation in TiO_2,[50] which is important for the catalytic systems studied here.

Formation energies and binding energies were calculated using:

$$\Delta E_f = E_{ads/Rh/TiO_2} - \left(E_{TiO_2} + E_{bulk} + E_{mol(g)}\right)$$

$$\Delta E_b = E_{ads/Rh/TiO_2} - \left(E_{Rh/TiO_2} + E_{mol(g)}\right)$$

Here ΔE_f is the formation energy of a single-atom-adsorbate complex (e.g., $Rh_1(CO)_2/TiO_2$), $E_{ads/Rh/TiO_2}$ is the DFT-calculated electronic energy of the single-atom-adsorbate complex, E_{TiO_2} is the energy of the TiO_2 surface (including an O vacancy, Ti vacancy, or OH group if present), E_{bulk} is the per-atom energy of Rh in the bulk face-centered cubic crystal, $E_{mol(g)}$ is the energy of the adsorbate molecule(s) in the gas phase, ΔE_b is the binding energy of an adsorbate to Rh_x/TiO_2, and E_{Rh/TiO_2} is the energy of the Rh_x/TiO_2 system itself. The bulk Rh was constructed using the optimized lattice constant of 3.816 Å (*a*, *b*, *c*).

The strength of the C–O bond for adsorbed CO was calculated as:

$$E_{C-O} = \left(E_{Rh-CO} + E_{H_2(g)}\right) - \left(E_{Rh-C} + E_{H_2O(g)}\right)$$

where E_{C-O} is the C–O bond energy, E_{Rh-CO} is the binding energy of CO on the supported Rh species, E_{Rh-C} is the binding energy of atomic C on Rh, and $E_{H_2(g)}$ and $E_{H_2O(g)}$ are the gas-phase electronic energies of hydrogen and water. Using this formula, the energy difference between bound CO and dissociated C and O is found, resulting in the C–O bond strength. H_2 and H_2O are chosen as the gas phase reference states for removing O from CO, since the reaction occurs under reducing conditions with plentiful $H_2(g)$.

Reported Gibbs free energies (ΔG) used in free energy diagrams and microkinetic modeling include ideal-gas corrections for molecular rotations, translations, and vibrations, as well as hindered rotation and vibration of the adsorbed species (as implemented in the ASE package).

Vibrational frequencies for Gibbs free energy calculations and for comparison with DRIFTS were computed within the harmonic approximation. The gas phase CO vibrational frequency calculated using PBE was 2103 cm^{-1}, which is about 40 cm^{-1} lower than the experimentally measured value of 2143 cm^{-1}.[51] For comparison with experimental DRIFTS measurements, a 40 cm^{-1} rigid shift was applied to all calculated vibrational frequencies for adsorbed CO to correct for this difference. Further modeling details are provided in the Supporting Information (SI).

Nanocluster geometry search. A genetic algorithm (GA) was used to search the structure of supported Rh_x nanoclusters ($x=4$–8 atoms) on anatase $TiO_2(101)$. The GA is based on an implementation in ASE.[52,53] The positions and structures of Rh_1, Rh_2, and Rh_3 on $TiO_2(101)$ were manually searched.

For each GA search, the starting population contained 12 randomly generated Rh_x structures. Next, DFT calculations were performed to evaluate the total electronic energy of each Rh_x structure in the population. All the atoms in Rh_x nanoclusters were relaxed during GA calculations, but a one-layer $TiO_2(101)$ support was fixed during the GA algorithm. Mutation and cross-over operations were applied to existing structures in the population to generate new structures.[52] The calculated total electronic energy was used to evaluate the fitness of each structure. The above steps were repeated to optimize the population of candidate nanoclusters. The GA was terminated if no new low-energy structures were found within 1000 attempts or after 80 generations, whichever came first. Repeated runs of the GA with different initial populations reidentified the same ground-state structures of the Rh_x nanoclusters. Final structures were re-optimized on a full 6-layer TiO_2 slab (changes in each cluster structure were minimal upon re-optimization). More details on the GA workflow are discussed in the SI and shown in Figure S1.

Microkinetic simulations. First-principles mean-field microkinetic simulations[54] of the rWGSR were conducted to predict TOFs, apparent activation barriers, and the degree of rate control (DRC)[55] for plausible Rh_1/TiO_2 sites and reaction mechanisms. All microkinetic simulations used the MKMCXX code.[56] The DFT-based microkinetic simulation approach that we use has been presented in detail elsewhere,[56,57] so here we summarize only the main points. The DFT-calculated forward and backward activation energies were used to calculate the rate constant of each elementary step. For surface reactions, the rate constant of step i was calculated using the Arrhenius equation. Differential equations for all the reaction species were built using the predicted rate and equilibrium constants and the set of elementary steps. The rates of the elementary steps were computed based on the steady-state coverages. Steady-state surface coverages were determined by integrating the differential equations in time until changes in the surface coverages were less than 10^{-8}. In our simulations, the gas phase consisted of CO_2 and H_2 in a 1:4 molar ratio at a total pressure of 1 atm, within the range of typical experimental reaction conditions.[58] Further microkinetic modeling details including the elementary steps of each studied rWGSR mechanism are provided in the SI.

Results and Discussion

Atomically Dispersed Rh_1 Catalysts for rWGSR

Rh_1 binding locations on TiO_2. The feasible Rh_1 binding locations must first be known to understand the activity and selectivity of Rh_1/TiO_2 toward the rWGSR. Atomically dispersed Rh_1 is known to change its coordination environment on anatase and rutile TiO_2 depending on the reaction conditions.[32,59] A recent study identified plausible sites for Rh_1 binding on anatase $TiO_2(101)$ under $CO+H_2$ reducing conditions using DFT and Fourier-transform infrared spectroscopy (FTIR), specifically $Rh_1(CO)_2$ bound to two, two-fold coordinated oxygen atoms (O_{2c}) with and without a nearby Ti–OH group.[32] Herein we build on this prior work and expand the set of structures considered as plausible Rh_1/TiO_2 sites, including anatase surfaces with oxygen vacancies and stepped sites.

We identify plausible binding locations for Rh_1 on anatase TiO_2 at zero Kelvin under vacuum based on DFT-computed formation energies and gem-dicarbonyl vibrational frequency analysis. The systems considered were: Rh_1 on clean $TiO_2(101)$, Rh_1 on the $TiO_2(134)$ step edge, Rh_1 occupying O vacancies at the two-fold coordinated (@O_{2c}vac) and three-fold coordinated (@O_{3c}vac) sites, Rh_1 occupying a Ti vacancy at the five-fold coordinated site (@Ti_{5c}vac), and Rh_1 with O vacancies nearby and far away. Rh_1 with a nearby hydroxyl group on TiO_2 [$Rh_1OH/TiO_2(101)$] as proposed by Asokan *et al.*[32] is also considered.

The bare Rh_1 systems considered are shown in the SI (Figure S2), which all have highly endothermic formation energies. In the presence of CO, the gem-dicarbonyl $Rh_1(CO)_2$ complexes (Figure 1) are much more stable than bare Rh_1 species. The $Rh_1(CO)_2$ are readily detected via DRIFTS to probe the Rh_1 site environments and thus are considered in detail for stability and vibrational frequency analysis.[60–64]

The $Rh_1(CO)_2$ formation energy on a defect-free $TiO_2(101)$ surface, where Rh_1 is bound through two surface oxygens (Figure 1a) is exothermic (−1.80 eV). This $Rh_1(CO)_2/TiO_2$ complex is the same structure as that suggested in recent work based on DRIFTS, temperature programmed desorption, and DFT.[32] Experimentally, the $Rh_1(CO)_2$ structure exhibits two peaks around 2097 and 2028 cm^{-1}, being the symmetric and asymmetric C–O bond stretches, respectively.[3,65] Vibrational stretches of 2080 cm^{-1} and 2027 cm^{-1} for $Rh_1(CO)_2$ on $TiO_2(101)$ (Figure 2) are predicted, similar to experiment and prior DFT vibrational frequency assignment.[32]

When considering a TiO_2 surface with nearby hydroxyl group (Rh_1OH), the Rh_1 binding location does not change from the clean surface (Figure 1b). The formation energy is also very exothermic (−3.06 eV). The calculated vibrational frequencies of 2093 cm^{-1} and 2026 cm^{-1} match closely with experimental values (Figure 2), differing only by 4 cm^{-1} and 1 cm^{-1}, respectively. These vibrational frequency predictions agree well with the prior study by Asokan *et al.*.[32]

In contrast, the formation energy of the $Rh_1(CO)_2/TiO_2(134)$ step edge is highly endothermic (0.91 eV, Figure 1c). Besides having an endothermic formation energy, $Rh_1(CO)_2/TiO_2(134)$ was also ruled out as an abundant surface species by incompatible vibrational frequencies compared with experiment (Figure 2), namely 1973 and 1941 cm^{-1}.

Examining the effect of oxygen vacancies on the Rh_1/TiO_2 system is important because they may participate in activating CO_2 for the rWGSR.[64,66,67] An oxygen vacancy would allow for an alternative mechanism for CO_2 dissociation into *CO and *O to heal the vacancy, bypassing any *COOH intermediate. Subsurface oxygen vacancies were measured by scanning tunneling microscopy in anatase TiO_2 under reducing conditions similar to those used for CO_2 reduction.[68,69] Supported Rh_1 has been

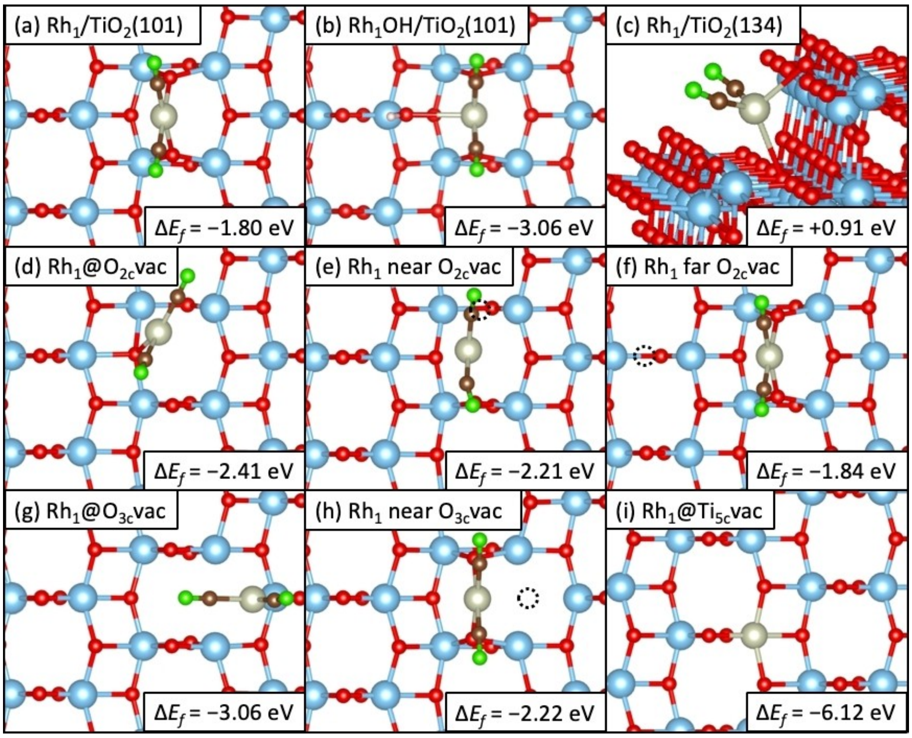

Figure 1. Top view of the gem-dicarbonyl $Rh_1(CO)_2$ binding locations on anatase TiO_2, along with their formation energy (ΔE_f) relative to a bare TiO_2 surface (defect-free, defective, or step, as relevant), Rh bulk lattice, and gaseous CO. The systems considered were: (a) Rh_1 on $TiO_2(101)$, (b) Rh_1 on $TiO_2(101)$ with a nearby hydroxyl group, (c) Rh_1 on the $TiO_2(134)$ step edge, (d) Rh_1 occupying an O vacancy at the two-fold coordinated site ($@O_{2c}vac$) on $TiO_2(101)$, (e) Rh_1 with an $O_{2c}vac$ nearby on $TiO_2(101)$, (f) Rh_1 with an $O_{2c}vac$ far away on $TiO_2(101)$, (g) Rh_1 occupying an O vacancy at the three-fold coordinated site ($@O_{3c}vac$) on $TiO_2(101)$, (h) Rh_1 near a $O_{3c}vac$ on $TiO_2(101)$ and (i) Rh_1 in a Ti vacancy at the five-fold coordinated site ($@Ti_{5c}vac$) on $TiO_2(101)$. Oxygen vacancies are denoted with dashed circles. Atom color legend: Blue = Ti, Red = O, Gray = Rh, Green = O in CO, Brown = C.

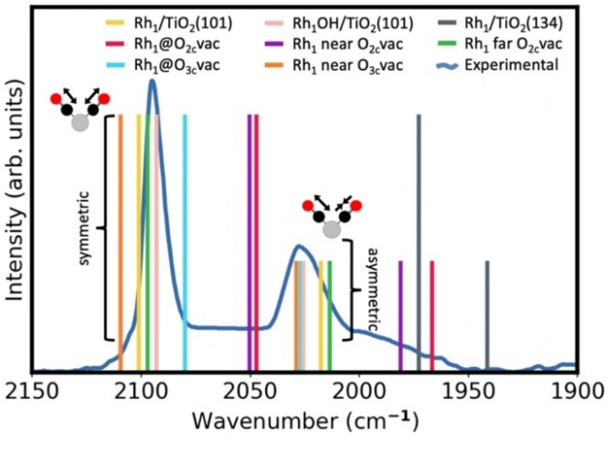

Figure 2. Experimental DRIFTS spectroscopy and DFT-predicted CO stretching frequencies under the harmonic approximation for $Rh_1(CO)_2$ systems. The two peaks observed are for symmetric (high intensity peak) and asymmetric (low intensity peak) stretches of CO. Note, only the peak positions as computed by DFT are reported and the intensities are arbitrarily specified for clarity. The experimental DRIFTS spectra (300 K, 10% CO/90% Ar) is reproduced from Ref. [3]. The experimental DRIFTS used P25, which is a mixture of 75% anatase and 25% rutile TiO_2.

shown via temperature programmed reduction to promote the formation of O vacancies within a P25 TiO_2 support, which is approximately 75% anatase and 25% rutile.[70] For (101) anatase, O vacancies were predicted by DFT to preferentially exist in the subsurface.[69,71] However, these O vacancies may diffuse throughout the lattice under reaction conditions.[71,72] Because of the mobility of O vacancies, both $O_{2c}vac$ (Figures 1d–f) and $O_{3c}vac$ (Figures 1g,h) surface vacancies are considered. The Rh_1 inside Ti vacancies (Figure 1i) likely have low abundance in the strong reducing environment of rWGSR. Further, the formation energy is strongly negative for Rh_1 filling Ti vacancies, and they are not predicted to form Rh_1–dicarbonyl complexes because of their saturated coordination environment;[32,59] thus we do not consider Ti vacancies further as active Rh_1 sites.

The data in Figure 2 shows calculated IR stretching frequencies for each considered $Rh_1(CO)_2/TiO_2$ system compared with experimental DRIFTS from Matsubu *et al.*[3] $Rh_1@O_{2c}vac$ or near an $O_{2c}vac$, and the $Rh_1/TiO_2(134)$ step edge all have frequencies far from experimentally observed values, and thus may not be present in appreciable abundance. Remaining plausible binding locations based on $Rh_1(CO)_2$ formation energies and vibrational frequency analysis are $Rh_1@O_{3c}vac$, Rh_1 near $O_{3c}vac$, Rh_1/TiO_2, and Rh_1OH/TiO_2. In particular, the Rh_1OH system agrees most closely with experiment, differing by less than 0.2% for both symmetric and asymmetric stretches. The $Rh_1/TiO_2(101)$ and $Rh_1OH/TiO_2(101)$ structures have been proposed previously as stable adsorption sites and potential active sites on anatase TiO_2,[32,33] but Rh_1 near $O_{3c}vac$ and $Rh_1@O_{3c}vac$

have not been studied in detail. In addition, with the exception of $Rh_1/TiO_2(101)$,[33] none of these species have had their rWGSR mechanism modeled via first-principles microkinetic modeling. We note that although CO-DRIFTS probes Rh_1 sites accessible by CO, which may be active sites for CO_2 reduction, it is possible that these sites are not fully representative of the distribution of sites present in CO_2+H_2 reaction conditions.

Microkinetic modeling of rWGSR on plausible Rh_1/TiO_2 active sites. Based on having exothermic gem-dicarbonyl formation energies and qualitative agreement with prior experimental CO-DRIFTS peak assignments, the $Rh_1/TiO_2(101)$, $Rh_1OH/TiO_2(101)$, $Rh_1@O_{3c}vac$, and Rh_1 near $O_{3c}vac$ are plausible active sites for rWGSR. However, we do not consider $Rh_1@O_{3c}vac$ further because CO_2 is weakly bound by this site, and the barrier for CO_2 dissociation is computed to be large (1.30 eV) compared to Rh_1 near $O_{3c}vac$ (0.21 eV). To clarify the activity differences among the remaining single-atom species, DFT-based microkinetic modeling of the rWGSR reaction mechanism is performed.

CO_2 hydrogenation to CO can proceed through a carboxyl intermediate (*COOH), which further reacts with *H to form water and CO. Alternatively, the $*CO_2$ can dissociate directly into *CO and *O by C–O bond cleavage, especially when *O is healing an oxygen vacancy on reducible supports such as CeO_2 and TiO_2.[58,73] In either case, *CO will desorb if not allowed to react further. The selectivity will depend on the binding strength of CO and the availability of nearby *H, both of which vary between Rh_1 and Rh_x.

The free energy diagrams for the rWGSR mechanisms of $Rh_1/TiO_2(101)$ and $Rh_1OH/TiO_2(101)$ are shown in Figure 3. The mechanism for $Rh_1/TiO_2(101)$ in Figure 3a is the same as the proposed mechanism by Ma and colleagues,[33] with H_2 and CO_2 adsorbing onto Rh_1, followed by H transfer to the oxygen within $*CO_2$ to form *COOH. The second hydrogen transfers to *COOH and reacts to form *CO and water, which is rate controlling (i.e., TS2 in Figure 3a, see Table S1 of SI for DRC analysis), where the water is weakly bound and desorbs from the surface. CO then desorbs to complete the cycle. An alternative mechanism was considered where bound *COOH dissociates to form *CO and *OH, followed by CO desorption and *OH hydrogenation to H_2O (Figure S3). This mechanism was predicted to have a lower reaction rate and led to a slightly higher apparent activation barrier.

The mechanism for Rh_1OH/TiO_2 in Figure 3b is modeled to form a hydroxyl group next to Rh_1 during the reaction that participates in CO_2 hydrogenation. The starting configuration is similar to that of $Rh_1/TiO_2(101)$, but with an extra O atom adjacent to Rh_1. H_2 adsorbs on Rh_1 and dissociates onto the nearby O, forming the *OH group and Rh–H. CO_2 then adsorbs, and the H bound to Rh_1 transfers to form *COOH. The remaining H of the OH group undergoes a two-step transfer by moving to Rh and then to *COOH to form *CO and H_2O, which is rate controlling (TS4 in Figure 3b, see Table S1 of SI for DRC analysis).

Both mechanisms share similarities, with a stable *COOH intermediate forming after one H transfer and a high barrier for the final H transfer to form H_2O. The activity of these two pathways is limited by the large free energy barrier to dissociate *COOH into CO and H_2O, with Rh_1OH further stabilizing the *COOH compared to the Rh_1 without a nearby hydroxyl group. The mechanism proposed here for Rh_1OH creates a system similar to that studied by Asokan *et al.*,[32] but it does not observe the same Rh_1OH with bound CO during the reaction itself. Instead, the H from OH is used to hydrogenate *COOH and leaves behind the O atom adjacent to Rh_1. This OH group may exist in different configurations under reaction conditions and CO-DRIFTS conditions.

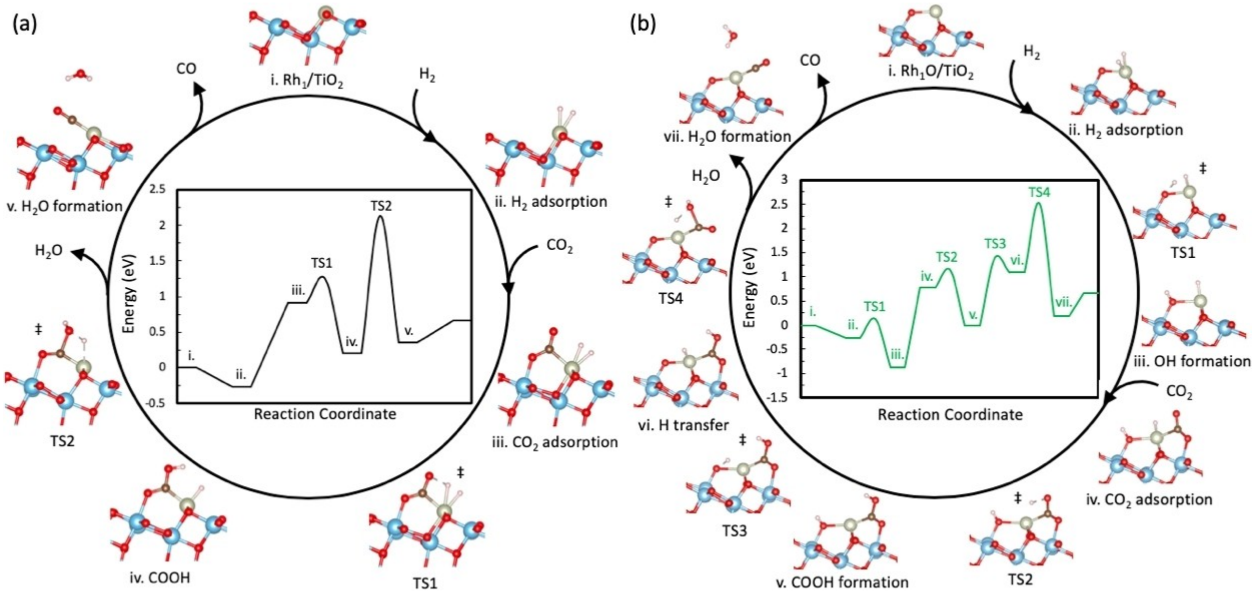

Figure 3. DFT-predicted free-energy diagrams for reverse water gas shift reaction by (a) $Rh_1/TiO_2(101)$ and (b) $Rh_1OH/TiO_2(101)$. Free energies were computed at 400 K and 1 atm total pressure. Atom color legend: Blue = Ti, Red = O, Gray = Rh, Brown = C, White = H.

The free energy diagram for the rWGSR mechanism of Rh_1 near O_{3c}vac is shown in Figure 4. The Rh_1 near O_{3c}vac mechanism begins similarly with H_2 adsorption, but then H_2 dissociates onto a nearby lattice oxygen (O_{3c}). When the remaining H reacts with the lattice OH, H_2O is formed and desorbs to leave an oxygen vacancy (O_{3c}vac), which is the step with the largest barrier (0.98 eV) and highest DRC (see Table S1). CO_2 then adsorbs with one of its oxygen atoms in the vacancy and dissociates to form CO, thereby healing the vacancy. CO desorbs to complete the cycle, as before. Elementary steps of each studied rWGSR mechanism on Rh_1/TiO_2, Rh_1OH/TiO_2, and Rh_1 near O_{3c}vac are provided in the SI.

The microkinetic model results in Figure 5a show the Rh_1 near O_{3c}vac system outperforming both the Rh_1 species on pristine TiO_2 and Rh_1 near a surface OH group with regards to predicted TOF. CO_2 reduction assisted via an oxygen vacancy has higher TOF by several orders of magnitude for the relevant temperature range of 400–600 K. Experimental observations show a TOF of $10^{-2.3}$ s^{-1} at 473 K, which is within an order of ~100 of the predicted TOF for Rh_1 near O_{3c}vac but 10^6–10^8 times too fast compared to $Rh_1/TiO_2(101)$ and $Rh_1OH/TiO_2(101)$. When comparing apparent activation barriers in Figure 5b, the vacancy system again displays relatively close agreement with experiment. The apparent activation barriers show maxima around 500 K due to a changing degree of rate control for *CO desorption. At higher temperature, *CO desorption becomes more favorable, and the apparent barrier begins to decrease.

Experimentally measured apparent activation barriers range from 1.24 eV at 393–423 K (0.5 wt% Rh, gas mixture 40% H_2, 10% CO_2, 50% He) and 1.07 eV at 473–573 K (0.5 wt% Rh, gas mixture 24% H_2, 6% CO_2, 70% He).[74,75] The $Rh_1/TiO_2(101)$ system has a predicted apparent barrier around 2.0–2.2 eV from 400–600 K, confirming that this previously proposed mechanism does not adequately represent the observed activity of the rWGSR on Rh_1/TiO_2. $Rh_1OH/TiO_2(101)$ likewise shares a high apparent activation barrier around 1.7–2.3 eV. In contrast, the Rh_1 near O_{3c}vac system barrier is 1.3–1.7 eV within the same temperature range, in much closer agreement with experiment.

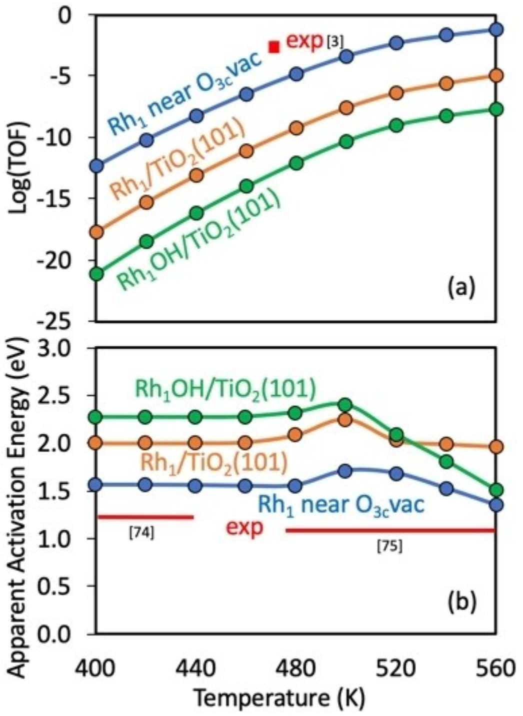

Figure 5. Predicted (a) TOF vs. temperature and (b) apparent activation energy vs. temperature for $Rh_1/TiO_2(101)$, Rh_1 near O_{3c}vac, and $Rh_1OH/TiO_2(101)$ based on mean-field microkinetic simulations. CO_2 and H_2 in a 1:4 molar ratio at a total pressure of 1 atm. Experimental data (exp) is shown inset from Ref. [3] for TOFs and Refs. [74,75] for apparent activation barriers over the denoted temperature range (solid red lines).

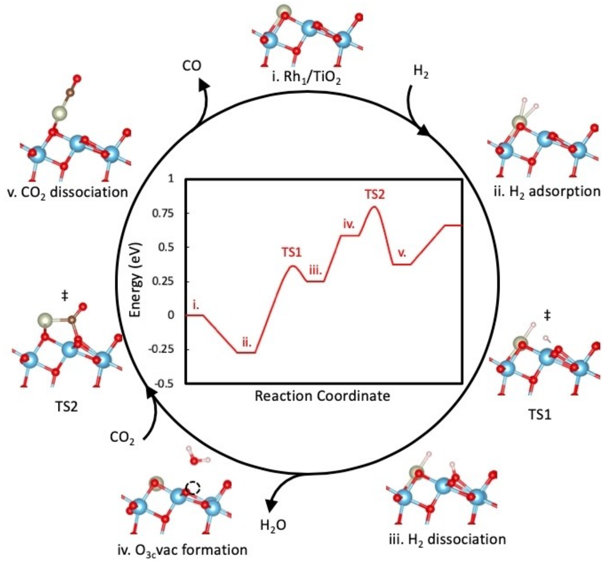

Figure 4. DFT-predicted free-energy diagrams for reverse water gas shift reaction by Rh_1 near O_{3c}vac, which proceeds via CO_2 dissociation assisted by a surface oxygen vacancy. Free energies were computed at 400 K and 1 atm total pressure. Atom color legend: Blue = Ti, Red = O, Gray = Rh, Brown = C, White = H.

The Rh_1 through an O_{3c}vac-assisted mechanism was predicted to have the closest agreement with experimental TOF and measured apparent activation barriers. This mechanism depends heavily on the availability of O vacancies at the surface of TiO_2, which will depend on the temperature and reducing conditions. While it is known that subsurface O vacancies are more stable than surface vacancies in anatase TiO_2,[69,76] it has also been suggested that the vacancies are mobile under reaction conditions.[71] Hence, subsurface O vacancies may still play a role in the binding and dissociation of CO_2 by cascading diffusion of O into the lattice. The O_{3c}vac-assisted mechanism shares similarities to what has been investigated for Rh_1 on rutile TiO_2, with oxygen vacancies promoting the direct dissociation of CO_2 to CO.[59]

It is important to note that the experimental samples that we compare against typically include 25% rutile TiO_2, which would offer different Rh_1 binding configurations and active sites, as well as a different abundance of surface oxygen vacancies. Rutile and anatase also exhibit differing amounts of electron transfer between metal and support, which in itself can reverse the observed selectivity.[77] Researchers may seek to minimize these variable support effects when studying rWGSR by using well-defined single atom binding sites such as polyoxometalates (POMs) as a model system for catalytic studies.[78]

Effect of Nanocluster Size on rWGSR Selectivity

The catalytic activity and selectivity of nanoclusters depend on their surface composition, shape, and size.[79–81] Therefore, representative structures of nanoclusters must be known to predict its catalytic performance. Finding the stable and relevant structures of supported metal nanoclusters requires a search of the configuration space, which can be achieved via a GA structure search[52,82,83] or other methods such as stochastic surface walking,[84] basin hopping,[85,86] or replica-exchange molecular dynamics.[87] A GA is selected here for its superior performance in finding the global minima of nanoclusters compared with methods such as simulated annealing.[88] We emphasize the structures identified here are model structures. The nanoclusters may change their size and shape under reaction conditions, which is not considered in our study. The structure of a given Rh nanocluster in equilibrium with some chemical potentials of reactants could in principle be addressed using techniques such as *ab initio* Grand Canonical Monte Carlo,[83,89] albeit this approach is computationally demanding for nanoclusters and multicomponent reaction conditions.

The predicted structures of the Rh_x single-atom and nanoclusters with one CO adsorbed are shown in Figure 6. No major structural rearrangements occurred upon CO adsorption compared with the bare clusters (Figure S4). The optimal CO adsorption configurations were found by sampling 19 different adsorption configurations distributed radially around each cluster (see SI for details). The Rh_2 and Rh_3 clusters are flat against the $TiO_2(101)$ surface with one layer of atoms, and the clusters of four atoms and above are two layers thick. In each case, the bottom layer of Rh atoms prefers to coordinate with oxygen in the TiO_2 lattice. Bader charge analysis of the atoms in the Rh nanocluster reveals that the atoms in the bottom layer have slight positive charge ($+0.01$ to $+0.55$ e) and the top layer atoms have slight negative charge (-0.01 to -0.11 e). Generally, the average Bader charge of the cluster decreases as size increases toward that of bulk Rh (Figure S5). CO binds most strongly to the cationic Rh–Rh bridge sites at the support interface, which aligns with prior knowledge that electron donors adsorb strongly to cationic sites at metal/support interfaces.[90,91] The cationic nature of metal atoms at the nanocluster/oxide interface is a well-known phenomenon for Rh/TiO_2[33,92] and other systems such as Pt/SiO_2,[93] Pt/Al_2O_3,[94] and Rh/faujasite.[95]

Atomically dispersed Rh_1 are quite cationic compared to nanoclusters (Figure 6). While positive charge is typically beneficial for binding electron donors such as CO, the metal–CO binding strength has been shown to vary on a case-by-case basis due to differences in coordination geometry and the extent of π-back-bonding occurring.[96] In our case, CO prefers to adsorb to Rh–Rh bridge sites on Rh nanoclusters, similarly to bulk Rh, which are not present for Rh_1. The presence of Rh–Rh bridge sites shows a stronger impact on CO binding than positive Bader charge alone. Weaker adsorption of CO on Rh_1 compared with nanoclusters should promote CO desorption before further hydrogenation to CH_4. The relatively weak adsorption of CO on Rh_1 compared with Rh nanoclusters is quite general based on DFT studies of CO adsorption[97] and CO temperature programmed desorption experiments on systems such as Pt/TiO_2,[16] Au/FeO,[98] and Rh/Al_2O_3.[99]

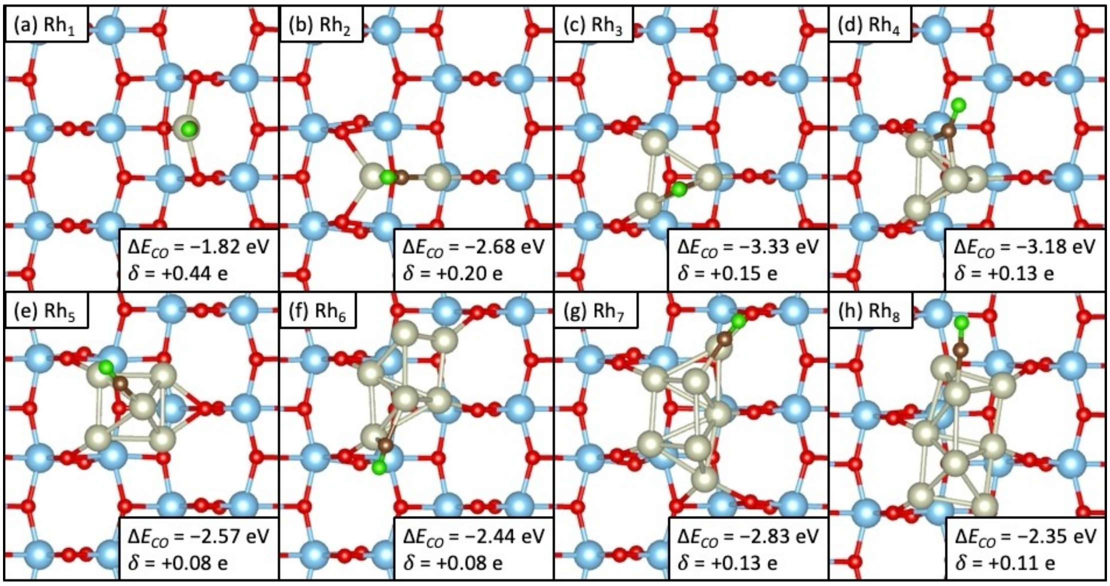

Figure 6. Most stable configurations of Rh_x/TiO_2 ($x=1$–8 atoms) with one CO adsorbed. The binding energy of CO (ΔE_{CO}) is given inset, as well as the average Bader charge (δ) of the Rh nanocluster atoms involved in the CO bond. Atom color legend: Blue = Ti, Red = O, Gray = Rh, Green = O in CO, Brown = C.

Our calculations predict that the binding energies of CO, CO_2, and H_2 are all relatively weak for Rh_1 compared with the larger Rh_x nanoclusters, Figure 7. The adsorbate chemisorption strength increases until Rh_3, then becomes weaker as nanocluster size further increases toward bulk Rh(111). For all cluster sizes, CO is bound more strongly than H_2 and CO_2, owing to its ability to participate in π-back-bonding with the Rh metal.[100] Regardless, all adsorbates follow a similar trend with cluster size, where adsorbate binding is strongest for small under-coordinated clusters that can still offer two- or three-fold sites.

We report a correlation between nanocluster size and the strength of the C–O bond for CO bound to each Rh nanocluster. Figure 7 shows that the C–O bond strength decreases from Rh_1 to larger Rh_x ($x=2$–8) nanoclusters and Rh(111). The high C–O bond strength for CO adsorbed on Rh_1 compared to nanoclusters is quantitatively similar for all considered Rh_1 sites (within 10% for Rh_1/TiO_2, Rh_1OH/TiO_2 and Rh_1 near O_{3c}vac). The C–O bond strength has been shown previously to be a descriptor of selectivity to CO for CO_2 reduction by Ir_1 species and nanoclusters.[97] For atomically dispersed catalysts such as Rh_1, in which C–O bond strength is larger than or similar to the CO binding energy, CO desorption is favored over further reduction. Because the C–O bond strength is weakened on Rh nanoclusters (including Rh_2 dimers) and Rh(111) compared to Rh_1 while having high CO adsorption strength, further reaction to products such as methane is favored over CO desorption. We have also investigated the CO binding and C–O bond strength trends for each cluster when a nearby O_{3c}vac is present. The overall trends are not strongly affected by the vacancy presence (Figure S8), indicating that the selectivity difference between Rh_1 and Rh_x holds across different support conditions.

Several examples in experimental studies show the importance of CO binding energy to selectivity.[97] For a Ru/TiO_2 catalyst, changing the support phase from rutile to anatase resulted in an increased amount of hydrogen migrating from metal to support, known as hydrogen spillover. This hydrogen spillover is accompanied by an electron transfer from metal to support, which weakened CO binding to Ru and caused a strong selectivity shift to rWGSR.[77] A related effect has also been observed for Rh/Al_2O_3 catalysts modified with Ni and K, where the Ni and K additives weaken the CO adsorption strength and hinder the rate of methanation.[101]

Another factor that may contribute to the increased CO_2-to-CO selectivity of Rh_1/TiO_2 is the lack of nearby metal sites to dissociate H_2.[3] To test this hypothesis, H_2 dissociation on Rh_2 dimers is predicted for comparison against Rh_1 on defect-free $TiO_2(101)$. H_2 bound to $Rh_1(CO)$ and $Rh_2(CO)$ are chosen as starting points because the methanation reaction depends on the further hydrogenation of bound CO. It is important to consider the CO already bound to Rh, since this would impact the ability to adsorb H_2 and is relevant to determining selectivity between rWGSR and methanation. The activation barrier for H_2 dissociation is calculated for the single atom and dimer systems.

The data in Figure 8 shows that the activation energy for H_2 dissociation on $Rh_1(CO)$ is higher than that of $Rh_2(CO)$ (0.90 vs 0.81 eV). Furthermore, H_2 does not adsorb nearly as strongly to $Rh_1(CO)$ compared with $Rh_2(CO)$ (−0.23 vs −1.09 eV), which has been hypothesized to arise from a lack of orbital overlap between $Rh_1(CO)$ and H_2.[33] The binding of H_2 is predicted to be weak and similar for all considered Rh_1 sites (i.e., Rh_1/TiO_2, Rh_1OH/TiO_2 and Rh_1 near O_{3c}vac). Consequently, Rh_1 species cannot readily dissociate H_2, in contrast to Rh_2 dimers. This phenomenon is similar to how Pd–Pd sites strongly adsorb H_2 and accelerate dissociative H_2 adsorption on a Pd/Au alloy, unlike Pd–Au sites that bind H_2 more weakly.[102,103] These results, combined with the findings that CO adsorbs weakly and has strong C–O bond strength on Rh_1 on TiO_2, explain the increased rWGSR selectivity of Rh_1 compared with Rh nanoclusters. These observations may also provide insight for other atomically dispersed metal ions and nanoclusters supported on metal oxides (e.g., Ru/Al_2O_3,[36] Pt/CeO_2,[14] Ru/CeO_2[15]) that

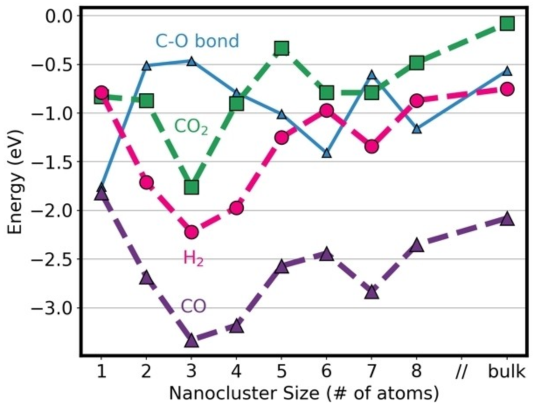

Figure 7. Binding energies (dashed lines) for gaseous species of interest (CO, H_2, CO_2) on Rh_x/TiO_2 ($x=1$–8 atoms). Also included is the strength of the C–O bond (solid line) for CO bound to each Rh_x cluster. Energies for the Rh(111) bulk system are provided as the upper limit for nanocluster size. More negative energy indicates a stronger bond. Binding energies for CO correspond to geometries in Figure 6, and those for CO_2 and H_2 are shown in Figure S6 and Figure S7.

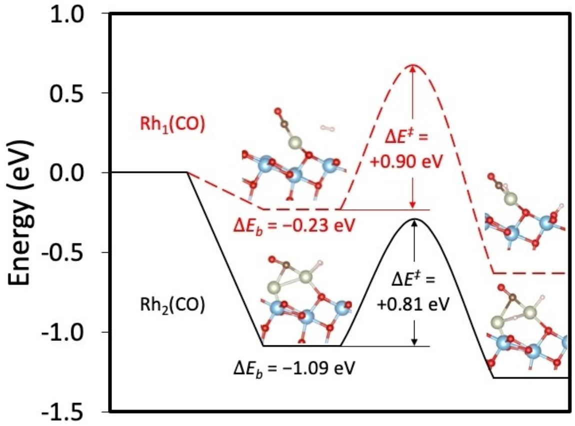

Figure 8. Adsorption and dissociation of H_2 on $Rh_1(CO)$ and $Rh_2(CO)$ supported on $TiO_2(101)$. The reference state is $Rh_1(CO)/TiO_2(101)$ or $Rh_1(CO)/TiO_2(101)$. ΔE_b is the electronic binding energy of H_2 on $Rh_x(CO)$ and $\Delta E^{\neq}$ is the activation energy for hydrogen dissociation.

display a similar rWGSR vs. methanation selectivity tradeoff for thermocatalytic CO_2 reduction.

Conclusions

The selectivity of thermocatalytic CO_2 reduction to CH_4 or CO depends strongly on the size of Rh species on TiO_2 under reducing conditions. The high CO selectivity of atomically dispersed Rh_1 catalysts on anatase TiO_2 compared with their larger Rh nanocluster counterparts has been experimentally demonstrated, but atomistic modeling of the origin of this selectivity difference has not yet been provided. Additionally, first-principles microkinetic modeling of Rh_1 active site(s) for CO_2 to CO reduction and the reaction pathway is lacking.

Here we computationally study plausible Rh_1/TiO_2 active sites and reaction mechanisms for CO_2 reduction to CO. We predict that Rh_1 on pristine TiO_2(101) (Rh_1/TiO_2(101)), Rh_1 with a nearby hydroxyl group on TiO_2 (Rh_1OH/TiO_2(101)), and Rh_1 near an oxygen vacancy at a three-fold coordinated site (Rh_1 near O_{3c}vac) are likely stable Rh_1 species. The relative abundance of these species will depend on the reaction conditions.[59] Among the considered Rh_1 sites and reaction mechanisms, a Rh_1 site on TiO_2(101) following CO_2 dissociation via an oxygen-vacancy assisted mechanism is predicted to be the most active toward CO production and had closest agreement compared with apparent activation barriers from literature.

Our findings reveal that CO adsorbs weakly and has strong C–O bond strength on Rh_1/TiO_2 compared with larger Rh_x ($x=$ 2–8 atoms) nanoclusters, including Rh_2 dimers. Also, Rh_1 has a larger activation barrier than Rh_2 dimers and nanoclusters to dissociate H_2 to reduce CO to CH_4 and does not have nearby Rh-metal sites to adsorb H*. Taken together these findings rationalize the unique capability of Rh_1 species to selectively catalyze CO_2 reduction to CO compared with Rh nanoclusters.

Associated Content

Supporting Information

Details on: DFT modeling of formation and binding energies, genetic algorithm, Rh_1/TiO_2 species and rWGSR reaction pathway modeling, and additional information on Rh nanocluster geometries and adsorbate binding are provided in the supporting information.

Acknowledgements

This work was partially supported by faculty start-up funds from the University of Michigan, Ann Arbor. BRG acknowledges partial support by the U.S. Department of Energy, Office of Science, Office of Fusion Energy Sciences General Plasma Science program under Award Number DE-SC-0020232. This research used resources of the National Energy Research Scientific Computing Center (NERSC), a U.S. Department of Energy Office of Science User Facility operated under Contract No. DE-AC02-05CH11231.

Conflict of Interest

The authors declare no conflict of interest.

Keywords: Single-Atom Catalyst · heterogeneous catalysis · CO2 Reduction · density functional theory · microkinetic modeling

[1] B. Qiao, A. Wang, X. Yang, L. F. Allard, Z. Jiang, Y. Cui, et al., *Nat. Chem.* **2011**, *3*, 634.

[2] Y. Kwon, T. Y. Kim, G. Kwon, J. Yi, H. Lee, *J. Am. Chem. Soc.* **2017**, *139*, 17694.

[3] J. C. Matsubu, V. N. Yang, P. Christopher, *J. Am. Chem. Soc.* **2015**, *137*, 3076.

[4] M.-M. Millet, G. Algara-Siller, S. Wrabetz, A. Mazheika, F. Girgsdies, D. Teschner, et al., *J. Am. Chem. Soc.* **2019**, *141*, 2451.

[5] X. F. Yang, A. Wang, B. Qiao, J. Li, J. Liu, T. Zhang, *Acc. Chem. Res.* **2013**, *46*, 1740.

[6] J. Liu, *ACS Catal.* **2017**, *7*, 34.

[7] S. C. Ammal, A. Heyden, *ACS Catal.* **2017**, *7*, 301.

[8] S. C. Ammal, A. Heyden, *ACS Catal.* **2019**, *9*, 7721.

[9] J. Shan, M. Li, L. F. Allard, S. Lee, M. Flytzani-Stephanopoulos, *Nature* **2017**, *551*, 605.

[10] H. Wang, J.-X. Liu, L. F. Allard, S. Lee, J. Liu, H. Li, et al., *Nat. Commun.* **2019**, *10*, 1.

[11] F. Doherty, H. Wang, M. Yang, B. R. Goldsmith, *Catal. Sci. Technol.* **2020**, *10*, 5772.

[12] J. Ma, N. Sun, X. Zhang, N. Zhao, F. Xiao, W. Wei, et al., *Catal. Today* **2009**, *148*, 221.

[13] C. Song, *Catal. Today* **2006**, *115*, 2.

[14] Y. Wang, H. Arandiyan, J. Scott, K.-F. Aguey-Zinsou, R. Amal, *ACS Appl. Mater. Interfaces* **2018**, *1*, 6781.

[15] A. Aitbekova, L. Wu, C. J. Wrasman, A. Boubnov, A. S. Hoffman, E. D. Goodman, et al., *J. Am. Chem. Soc.* **2018**, *140*, 13736.

[16] L. DeRita, S. Dai, K. Lopez-Zepeda, N. Pham, G. W. Graham, X. Pan, et al., *J. Am. Chem. Soc.* **2017**, *139*, 14150.

[17] J. Resasco, L. DeRita, S. Dai, J. P. Chada, M. Xu, X. Yan, et al., *J. Am. Chem. Soc.* **2020**, *142*, 169.

[18] M. J. Hülsey, B. Zhang, Z. Ma, H. Asakura, D. A. Do, W. Chen, et al., *Nat. Commun.* **2019**, *10*, 1330.

[19] C. Wang, X.-K. Gu, H. Yan, Y. Lin, J. Li, D. Liu, et al., *ACS Catal.* **2017**, *7*, 887.

[20] H. Yan, H. Cheng, H. Yi, Y. Lin, T. Yao, C. Wang, et al., *J. Am. Chem. Soc.* **2015**, *137*, 10484.

[21] M. A. Newton, C. Belver-Coldeira, A. Martínez-Arias, M. Fernández-García, *Nat. Mater.* **2007**, *6*, 528.

[22] A. J. Dent, J. Evans, S. G. Fiddy, B. Jyoti, M. A. Newton, M. Tromp, *Angew. Chem. Int. Ed.* **2007**, *46*, 5356.

[23] A. Berkó, J. Szökő, F. Solymosi, *Surf. Sci.* **2004**, *566–568*, 337.

[24] F. Solymosi, M. Pasztor, *J. Phys. Chem.* **1985**, *89*, 4789.

[25] Takanori. Mizushima, Kazuyuki. Tohji, Yasuo. Udagawa, Akifumi. Ueno, *J. Phys. Chem.* **1990**, *94*, 4980.

[26] B. R. Goldsmith, E. D. Sanderson, R. Ouyang, W. X. Li, *J. Phys. Chem. C* **2014**, *118*, 9588.

[27] R. Ouyang, J.-X. Liu, W.-X. Li, *J. Am. Chem. Soc.* **2013**, *135*, 1760.

[28] A. Berkó, F. Solymosi, *J. Catal.* **1999**, *183*, 91.

[29] J. Evans, B. Hayden, F. Mosselmans, A. Murray, *Surf. Sci.* **1994**, *301*, 61.

[30] J. Evans, B. Hayden, F. Mosselmans, A. Murray, *Surf. Sci. Lett.* **1992**, *279*, L159.

[31] M. Frank, R. Kühnemuth, M. Bäumer, H.-J. Freund, *Surf. Sci.* **1999**, *427–428*, 288.

[32] C. Asokan, H. V. Thang, G. Pacchioni, P. Christopher, *Catal. Sci. Technol.* **2020**, *10*, 1597.

[33] S. Ma, W. Song, B. Liu, H. Zheng, J. Deng, W. Zhong, et al., *Catal. Sci. Technol.* **2016**, *6*, 6128.

[34] I. V. Chernyshova, P. Somasundaran, S. Ponnurangam, *Proc. Nat. Acad. Sci.* **2018**, *115*, E9261.
[35] O. R. Luca, A. Q. Fenwick, *J. Photochem. Photobiol. B* **2015**, *152*, 26.
[36] J. H. Kwak, L. Kovarik, J. Szanyi, *ACS Catal.* **2013**, *3*, 2449.
[37] J. Lin, A. Wang, B. Qiao, X. Liu, X. Yang, X. Wang, et al., *J. Am. Chem. Soc.* **2013**, *135*, 15314.
[38] G. Kresse, J. Hafner, *Phys. Rev. B* **1993**, *47*, 558.
[39] G. Kresse, J. Furthmüller, *Comput. Mater. Sci.* **1996**, *6*, 15.
[40] G. Kresse, J. Furthmüller, *Phys. Rev. B* **1996**, *54*, 11169.
[41] G. Kresse, D. Joubert, *Phys. Rev. B* **1999**, *59*, 11.
[42] M. R. Ranade, A. Navrotsky, H. Z. Zhang, J. F. Banfield, S. H. Elder, A. Zaban, et al., *Proc. Nat. Acad. Sci.* **2002**, *99*, 6476.
[43] A. Vittadini, M. Casarin, A. Selloni, *Theor. Chem. Acc.* **2007**, *117*, 663.
[44] R. Hengerer, B. Bolliger, M. Erbudak, M. Grätzel, *Surf. Sci.* **2000**, *460*, 162.
[45] A. H. Larsen, J. Jens, J. Blomqvist, *J. Phys. Condens. Matter* **2017**, *29*, 273002.
[46] L. Iyengar, K. V. K. Rao, S. V. N. Naidu, *J. Am. Ceram. Soc.* **1969**, *53*, 124.
[47] G. Henkelman, B. P. Uberuaga, H. Jónsson, *J. Chem. Phys.* **2000**, *113*, 9901.
[48] S. Grimme, J. Antony, S. Ehrlich, H. Krieg, *J. Chem. Phys.* **2010**, *132*.
[49] B. J. Morgan, G. W. Watson, *Surf. Sci.* **2007**, *601*, 5034.
[50] Z. Hu, H. Metiu, *J. Phys. Chem. C* **2011**, *115*, 5841.
[51] N. Mina-Camilde, C. Manzanares, J. F. Caballero, *J. Chem. Educ.* **1996**, *73*, 804.
[52] L. B. Vilhelmsen, B. Hammer, *J. Chem. Phys.* **2014**, *141*, 044711.
[53] S. R. Bahn, K. W. Jacobsen, *Comput. Sci. Eng.* **2002**, *4*, 56.
[54] A. Bruix, J. T. Margraf, M. Andersen, K. Reuter, *Nat. Catal.* **2019**, *2*, 659.
[55] C. T. Campbell, *ACS Catal.* **2017**, *7*, 2770.
[56] I. A. W. Filot, R. J. P. Broos, J. P. M. van Rijn, G. J. H. A. van Heugten, R. A. van Santen, E. J. M. Hensen, *ACS Catal.* **2015**, *5*, 5453.
[57] J.-X. Liu, D. Richards, N. Singh, B. R. Goldsmith, *ACS Catal.* **2019**, *9*, 7052.
[58] M. D. Porosoff, B. Yan, J. G. Chen, *Energy Environ. Sci.* **2016**, *9*, 62.
[59] Y. Tang, C. Asokan, M. Xu, G. W. Graham, X. Pan, P. Christopher, et al., *Nat. Commun.* **2019**, *10*, 1.
[60] J. T. Yates, T. M. Duncan, R. W. Vaughan, *J. Chem. Phys.* **1979**, *71*, 9.
[61] J. T. Yates, T. M. Duncan, S. D. Worley, R. W. Vaughan, *J. Chem. Phys.* **1979**, *70*, 1219.
[62] H. Miessner, I. Burkhardt, D. Gutschick, A. Zecchina, C. Morterra, G. Spoto, *J. Chem. Soc. Faraday Trans. 1 Phys. Chem. Condens. Phases* **1989**, *85*, 2113.
[63] S. Trautmann, M. Baerns, *J. Catal.* **1994**, *150*, 335.
[64] J. Rasko, F. Solymosi, *J. Phys. Chem.* **1994**, *98*, 7147.
[65] M. Frank, R. Kühnemuth, M. Bäumer, H.-J. Freund, *Surf. Sci.* **2000**, *454–456*, 968.
[66] Y. Ji, Y. Luo, *J. Am. Chem. Soc.* **2016**, *138*, 15896.
[67] É. Novák, K. Fodor, T. Szailer, A. Oszkó, A. Erdöhelyi, *Top. Catal.* **2002**, *20*, 107.
[68] X. Pan, M.-Q. Yang, X. Fu, N. Zhang, Y.-J. Xu, *Nanoscale* **2013**, *5*, 3601.
[69] Y. He, O. Dulub, H. Cheng, A. Selloni, U. Diebold, *Phys. Rev. Lett.* **2009**, *102*, 106105.
[70] H. Guan, J. Lin, B. Qiao, S. Miao, A.-Q. Wang, X. Wang, et al., *AIChE J.* **2017**, *63*, 2081.
[71] P. Scheiber, M. Fidler, O. Dulub, M. Schmid, U. Diebold, W. Hou, et al., *Phys. Rev. Lett.* **2012**, *109*, 136103.
[72] M. Setvín, U. Aschauer, P. Scheiber, Y.-F. Li, W. Hou, M. Schmid, et al., *Science* **2013**, *341*, 988.
[73] S. Kattel, B. Yan, J. G. Chen, P. Liu, *J. Catal.* **2016**, *343*, 115.
[74] A. Karelovic, P. Ruiz, *J. Catal.* **2013**, *301*, 141.
[75] Z. L. Zhang, A. Kladi, X. E. Verykios, *J. Catal.* **1994**, *148*, 737.
[76] H. Cheng, A. Selloni, *Phys. Rev. B* **2009**, *79*, 092101.
[77] X. Li, J. Lin, L. Li, Y. Huang, X. Pan, S. E. Collins, et al., *Angew. Chem. Int. Ed.* **2020**, *59*, 19983.
[78] M. J. Hülsey, G. Sun, P. Sautet, N. Yan, *Angew. Chem. Int. Ed.* **2021**, *60*, 4764.
[79] H. Zhai, A. N. Alexandrova, *ACS Catal.* **2017**, *7*, 1905.
[80] A. Sanchez, S. Abbet, U. Heiz, W.-D. Schneider, H. Häkkinen, R. N. Barnett, et al., *J. Phys. Chem. A* **1999**, *103*, 9573.
[81] A. T. Bell, *Science* **2003**, *299*, 1688.
[82] P. C. Jennings, S. Lysgaard, J. S. Hummelshøj, T. Vegge, T. Bligaard, *Npj Comput. Mater.* **2019**, *5*, 46.
[83] J.-X. Liu, Y. Su, I. A. W. Filot, E. J. M. Hensen, *J. Am. Chem. Soc.* **2018**, *140*, 4580.
[84] C. Shang, Z.-P. Liu, *J. Chem. Theory Comput.* **2013**, *9*, 1838.
[85] D. J. Wales, J. P. K. Doye, *J. Phys. Chem. A* **1997**, *101*, 5111.
[86] G. G. Rondina, J. L. F. Da Silva, *J. Chem. Inf. Model.* **2013**, *53*, 2282.
[87] Y. Sugita, Y. Okamoto, *Chem. Phys. Lett.* **1999**, *314*, 141.
[88] D. M. Deaven, K. M. Ho, *Phys. Rev. Lett.* **1995**, *75*, 288.
[89] R. B. Wexler, T. Qiu, A. M. Rappe, *J. Phys. Chem. C* **2019**, *123*, 2321.
[90] W. T. Wallace, R. L. Whetten, *J. Phys. Chem. B* **2000**, *104*, 10964.
[91] S. Kattel, P. Liu, J. G. Chen, *J. Am. Chem. Soc.* **2017**, *139*, 9739.
[92] C.-T. Yang, B. C. Wood, V. R. Bhethanabotla, B. Joseph, *J. Phys. Chem. C* **2014**, *118*, 26236.
[93] C. S. Ewing, M. J. Hartmann, K. R. Martin, A. M. Musto, S. J. Padinjarekutt, E. M. Weiss, et al., *J. Phys. Chem. C* **2015**, *119*, 2503.
[94] A. Beniya, S. Higashi, N. Ohba, R. Jinnouchi, H. Hirata, Y. Watanabe, *Nat. Commun.* **2020**, *11*, 1.
[95] G. N. Vayssilov, B. C. Gates, N. Rösch, *Angew. Chem. Int. Ed.* **2003**, *42*, 1391.
[96] Z. Jakub, J. Hulva, M. Meier, R. Bliem, F. Kraushofer, M. Setvin, et al., *Angew. Chem.* **2019**, *131*, 14099.
[97] X. Chen, X. Su, H.-Y. Su, X. Liu, S. Miao, Y. Zhao, et al., *ACS Catal.* **2017**, *7*, 4613.
[98] Sh. K. Shaikhutdinov, R. Meyer, M. Naschitzki, M. Bäumer, H.-J. Freund, *Catal. Lett.* **2003**, *86*, 211.
[99] D. N. Belton, S. J. Schmieg, *Surf. Sci.* **1988**, *202*, 238.
[100] G. Blyholder, *J. Phys. Chem.* **1964**, *68*, 2772.
[101] D. Heyl, U. Rodemerck, U. Bentrup, *ACS Catal.* **2016**, *6*, 6275.
[102] W.-Y. Yu, G. M. Mullen, C. B. Mullins, *J. Phys. Chem. C* **2013**, *117*, 19535.
[103] F. R. Lucci, M. T. Darby, M. F. G. Mattera, C. J. Ivimey, A. J. Therrien, A. Michaelides, et al., *J. Phys. Chem. Lett.* **2016**, *7*, 480.

Manuscript received: February 24, 2021
Revised manuscript received: April 16, 2021
Accepted manuscript online: April 20, 2021
Version of record online: May 22, 2021